Journal of Alloys and Compounds 1062 (2026) 187626

Contents lists available at ScienceDirect

Journal of Alloys and Compounds

journal homepage: www.elsevier.com/locate/jalcom

Mechanism for step-mediated partitioning in Si-Ge rapidly solidified from its parent melt

Osama Al-Jenabi [a,b,c,*], Ahmed Nassar [d], Robert F. Cochrane [c], Andrew M. Mullis [c]

[a] Renewable Energy Research Centre, University of Anbar, Ramadi, Iraq
[b] School of Mechanical Engineering, University of Leeds, Leeds LS2 9JT, UK
[c] School of Chemical & Process Engineering, University of Leeds, Leeds LS2 9JT, UK
[d] Brunel Centre for Advanced Solidification Technology (BCAST), Brunel University London, Uxbridge UB8 3PH, UK

ARTICLE INFO

Keywords:
SiGe
Rapid solidification
Superlattices
Strain Mapping
Lattice distortion
HRTEM

ABSTRACT

We investigate the partitioning behaviour of a Si-30 wt% Ge alloy solidified from its parent melt, both close to equilibrium and under rapid solidification conditions. Contrary to the isomorphous equilibrium phase diagram, we observe step-mediated partitioning, with a number of discrete, Ge-rich, compositions occurring in the grain boundary region. The extent of this heterogeneity becomes greater as the cooling rate increases, with little evidence for solute trapping. Three such step-mediated interfaces are investigated using transmission electron microscopy across a range of cooling rates from $< 1\ s^{-1}$ to in excess of 25000 s^{-1}. Selected area electron diffraction patterns indicate that in all cases the more Ge-rich phase is chemically ordered, again at variance with the equilibrium phase diagram. High-resolution transmission electron microscopy imaging and geometric phase analysis are used to investigate the strain state of these interfaces, leading us to believe that step-mediated partitioning is a means of minimising the lattice strain arising from the atomic size difference between Si and Ge. This is known behaviour in Si-Ge thin films but has gone largely unrecognised in bulk Si-Ge material.

1. Introduction

Silicon germanium alloys, of the form $Si_{1-x}Ge_x$, are technologically important in several applications due to their tuneable properties. They are employed in optoelectronics, where the bandgap can be adjusted via composition to target specific optical wavelengths for photodetectors and infrared sensing [1]. They are also widely used in microelectronics, particularly in high-speed, low-power integrated circuits, where bandgap engineering and strain modulation can enhance carrier mobility and device performance [2]. However, it is as an efficient thermoelectric material for high temperature applications [3–7] that Si-Ge alloys show most promise, particularly for energy recovery during steel-making [4,8]. However, strong partitioning of Ge during solidification leads to a typical structure comprising Si-rich grains with Ge-rich grain boundaries, the converse of the chemically homogeneous structure required for good thermoelectric performance. One route that has been suggested to reduce this solidification induced heterogeneity is rapid quenching of the melt, which in most other materials results in improved homogeneity and a fine grained microstructure [3]. In this regard, both melt spinning and drop-tube processing have been investigated as potential routes for the rapid solidification processing of SiGe thermoelectric alloys [4,9]. However, recent evidence introduced by Hussain, et al. [4] suggests the formation of fixed stoichiometries in the Ge-rich grain boundary region, rather than the continuous graduation in Ge-concentration that would be expected from a system with an isomorphous equilibrium phase diagram.

The formation of compound-like regions in rapidly solidified Si–14.2 at% Ge material was recently studied by Hussain, et al. [4] and Al-Jenabi, et al. [7], with regions of fixed stoichiometry including Ge_3Si_2 and Ge_1Si_4 being identified. Hussain, et al. [4] observed that the concentration steps (i.e. the degree of inhomogeneity) associated with these compound-like regions became greater as the cooling rate is increased. A similar Ge-segregation pattern was observed by Al-Jenabi, et al. [7], who also noted that these fixed stoichiometries display compositions that occur only in integer multiples of 5 at% Ge. Al-Jenabi, et al. also observed that the more Ge-rich regions displayed chemical ordering, as witnessed by the presence of superlattice spots in selected area electron diffraction (SAED) patterns obtained from transmission electron microscopy (TEM) of rapidly solidified SiGe. These studies collectively challenge the traditional understanding of alloy solidification behaviour

---

[*] Corresponding author at: Renewable Energy Research Centre, University of Anbar, Ramadi, Iraq.
E-mail addresses: mnoij@leeds.ac.uk, oiabd@uoanbar.edu.iq (O. Al-Jenabi).

https://doi.org/10.1016/j.jallcom.2026.187626
Received 27 November 2025; Received in revised form 14 March 2026; Accepted 26 March 2026

in Si-Ge.

Beyond the expectations derived from equilibrium phase diagrams, the microstructural evolution of Si–Ge alloys is strongly influenced by both cooling rate and spatial confinement. Gumennik, et al. [10] studied the solidification of isolated, micron scale Si-Ge droplets confined by capillary break-up within a silica rod. Subsequent melting by means of laser irradiation resulted in both conventional dendritic microstructures and Janus type particles. This latter, where the face of the particle illuminated by the laser is distinctly different to that facing away from the laser, likely arises due to planar front solidification, possibly mediated by the confinement of the droplet, wherein stresses exceeding 1 GPa were encountered. The formation of such Janus particles may reflect Aperiodic Stepwise Growth [11] in these materials, wherein partitioning is influenced by the crystallographic orientation of the growing solid, with some orientations in single crystal droplets preferentially rejecting Ge, leading to accumulation of Ge in the last liquid to solidify near the point of laser contact. Conversely, Evans, et al. [12] studied solidification in 5–200 nm Si-Ge droplets, wherein cooling rates for the smallest droplets were sufficient to produce fully amorphous structures, comprising a tetrahedrally coordinated covalent random network structure.

Welch, et al. [13] applied laser additive manufacture to Si-Ge powders, wherein cooling rates are not dissimilar to those found in drop-tube experiments. They found that for $Si_{80}Ge_{20}$ alloys, as in the drop-tube experiments of [4,7], Si-rich dendritic grains were formed with Ge concentrated at the grain boundaries. They also observed a high density of dislocations at phase boundaries and diffraction spots which they associated with the formation of nanoscale intermetallic precipitates, although they were unable to determine the composition of these. Interestingly, they speculated that the presence of both these precipitates and of dislocations and point defects may aid the thermoelectric performance of the Si-Ge alloy.

As noted by Ghosh, et al. [14,15] this propensity for Ge to form a range of stoichiometric compounds upon non-equilibrium solidification from the melt appears not to be limited to its addition to Si, with Al-Ge alloys forming a range of such compounds under rapid solidification conditions during laser additive manufacture. However, this complexity of microstructures observed upon solidification appears to be contrary to the situation observed in the growth of the solid from the vapour, wherein for instance Tomasini [16] states that "$Si_{1-x}Ge_x$ growth mechanism appears identical across chemistries and crystal planes".

The occurrence of severe segregation with a graded composition change, known as step-mediated segregation, is well documented in SiGe thin films. Moreover, strain is one of the most significant factors affecting the properties of superlattice based devices [17,18]. According to work by Araki, et al. [19], the suggested mechanism for chemical ordering in SiGe thin films is strain-enhanced diffusion, wherein the strain energy arising from lattice distortion enhances the formation the stable, chemically ordered structures, with such chemical ordering being mediated by the formation of rhombohedral structures [20]. However, this concept has not been explored in bulk SiGe alloys solidified directly from their parent melt. In this paper we explore the critical role strain across Ge-rich grain boundaries plays in the development of stoichiometric, compounds-like regions in rapidly solidified SiGe alloy.

High-resolution transmission electron microscopy (HRTEM) imaging is a powerful tool for determining crystallographic information such as crystal structure, orientation and the presence of defects in semiconductors material [5,18,21]. One of the main techniques for measuring and mapping lattice displacements and strain fields from HRTEM micrographs is geometric phase analysis (GPA), based upon the comparison of HRTEM image features with a two-dimensional reference lattice to establish the lattice distortion within the micrograph. Local distortions are applied to find the local strain distribution of the crystal [21].

In this paper we investigate the lattice distortion and residual strain fields in three $Si_{70}Ge_{30}$ samples solidified under very different cooling regimes to determine whether such lattice strain plays a role in the observed step-mediated segregation observed in bulk SiGe alloys. Two of these samples were solidified via drop-tube processing and are taken from the > 850-μm and 150–106 μm particle size fractions and as such will have experienced intermediate and high cooling rates respectively. The third sample was recovered from the unejected material in the drop-tube crucible, and will have experienced a very low cooling rate during controlled cooling of the drop-tube furnace at the end of the experiment. Our focus lies in employing HRTEM imaging for comparative analysis of the interface between different step-concentration regions in each of the three samples. We undertake an analysis of lattice distortion measurements and strain mapping, particularly along the Ge-rich/SiGe interface, including GPA analysis across the step-concentration interfaces in each of the three samples.

2. Experimental sections

2.1. Fabrication of SiGe droplets by drop-tube processing

Pre-alloyed Si–14.2 at% Ge was obtained from Goodfellow in solid lump form, with this being crushed into small pieces, with a total mass of around 4.2 g, for subsequent processing. Rapid solidification of the SiGe alloy was achieved using a 6.5 m, high vacuum drop-tube. The pre-alloyed material is loaded into an alumina crucible which has three laser-drilled holes in the bottom, each being around 300 μm in diameter. These holes allow the ejection of melt that then solidify in-flight into fine particles. The alumina crucible, together with a graphite susceptor, are protected by a twin-walled alumina heat-shield, with the whole furnace assembly being positioned inside an induction coil connected to a 3 kW radio frequency (RF) power source.

The drop-tube is evacuated by pumping through two stages. Firstly, a rough pump is used to create a vacuum of 6.8×10^{-3} mbar before the tube is filled with oxygen-free N_2 gas to a pressure of 500 mbar, with this pump-flush cycle being repeated three times. Secondly, a turbomolecular pump is used to evacuate the tube to a pressure of 1.9×10^{-5} mbar before again being filled to 500 mbar with nitrogen gas. An R-type thermocouple is used to record the temperature of the melt during RF heating. As a consequence of this RF heating, the alloy is subjected to strong electromagnetic stirring during melting, this continuing up to and including the point of melt ejection into the drop tube. This ensures thorough homogenisation of the molten alloy prior to ejection, effectively eliminating large-scale compositional inhomogeneity in the starting melt within the crucible.

To ensure complete melting prior to melt ejection, the crucible was surrounded by a graphite susceptor that absorbs RF power and provides radiative heating to the sample. At the end of a 130-minute heating cycle, an estimated superheat of ~50 K above the liquidus temperature was applied to promote melt homogeneity. The thermocouple arrangement measures the radiation temperature within the crucible, confirming adequate superheating of the melt. The melt is then ejected from the crucible by pressurising with 4 bar of N_2 gas. The resulting alloy droplets were sieved into eight standard size fractions, of which two, 150–106 μm and > 850-μm, were selected for TEM analysis. The largest size fraction corresponds to the > 850 μm sieve; in practice, its upper size is limited to < 1000 μm as larger droplets do not fully solidify in flight and are collected as non-spherical splats or ribbons, which are manually removed. Only spherical or near-spherical particles are collected, defining an analyzed range of 850–1000 μm for the largest fraction. The cooling rate for each sieve fraction is calculated via the heat balance model presented by Oloyede, et al. [22]. In addition, some unejected material is retained at the base of the crucible, and this has a well-defined cooling rate as the drop-tube furnace is cooled at 10 K min^{-1} in order to prevent damage to the alumina heat shield.

For most materials the stochastic nature of the nucleation process means that particles of similar diameter may experience different undercoolings, resulting in different phases or microstructural morphologies within a given size fraction. However, in rapidly solidified Si–Ge this does not appear to be the case, as reported by Hussain, et al. [4] and Al-Jenabi, et al. [7]. Across all size fractions investigated only one morphology that of large Si-rich grains with much more Ge-rich grain boundaries, is observed. Variations within a size fraction are small and systematic, and therefore explicit screening of "ideal" particles was not required.

2.2. Characterizations

Following sieving, the powder samples were mounted in two-part epoxy resin and ground using a series of progressively finer SiC grinding papers ranging from P240 to P1200 grit, with optical microscopy being used to check the quality of the surface finish at each stage. The ground samples then were polished using 6, 3 and 1 μm diamond paste, with the samples being washed using dilute detergent and propanol and then dried using hot air between each polishing step. For SEM backscatter imaging, a Buehler Automat 250 grinding-polishing machine was used to perform a final polishing step using 0.05 μm colloidal silica suspension for 5 min to improve the surface finish. The polishing settings used during this stage were force = 20 N, speed of base = 140 rpm and speed of head = 50 rpm. Given the good backscatter contrast between Si and Ge due to their differing atomic number, there was no requirement to etch the samples.

For TEM analysis, sections < 100 nm in thickness were milled with high-energy Ga^+ ions using an FEI Helios G4 FEGSEM focused ion beam (FIB). Samples were selected so as to include a range of distinct structures across the Ge-rich grain boundaries from three samples, two drop-tube powders (>850 and 150–106 μm sieve fractions) and the crucible residual material, which is used to provide a slow cooling reference. For FIB/TEM analysis, a single representative particle from the 150–106 μm and > 850 μm sieve fractions was selected for cross-sectional examination. To ensure analysis of a representative equatorial region, selected particles exhibited (1) no visual indication of being a small surface cap, confirming that the majority of the particle lay below the polished surface, and (2) an apparent surface diameter within the expected sieve range (e.g., >106 μm for the 150–106 μm fraction). The specific particles analyzed had apparent surface diameters of ~128 μm (106–150 μm fraction) and ~930 μm (>850 μm fraction) (see panel (a) in Figure S1 and Figure S2). These 2D cross-sectional measurements are provided to document the sampled particles; the primary size classification remains the sieved fraction.

To ensure that the FIB sampling positions are representative of the overall droplet microstructure, SEM images of whole droplets were examined prior to sampling. Figure S1 shows a > 850 μm droplet and Figure S2 shows a 150–106 μm droplet, with the selected FIB regions indicated. These images, consistent with observations reported by Hussain, et al. [4], Al-Jenabi, et al. [7], and Al-Jenabi [23], confirm that the solidification structure does not exhibit any systematic near-surface bias and that the selected FIB sections accurately reflect the bulk droplet microstructure.

TEM analysis consisted of bright-field imaging, energy dispersive X-ray spectroscopy (EDX) line scans and mapping, along with SAED analysis which are used for strain mapping. Analysis was conducted using an FEI Titan Themis TEM operating at 300 kV. Bright field (BF) images were acquired with a Gatan OneView 16-megapixel CMOS digital camera. The Super-X EDX system, employing a windowless 4-detector design, facilitated EDX mapping and line scans through the Velox 2.4 software. SAED patterns for Ge-rich, intermediate, and Si-rich regions were indexed using ICDD crystallographic data files with references 01–071–4636, 04–008–2206, and 04–006–2527, respectively. Automatic indexing was performed using the SingleCrystal software package.

2.3. Strain measurements from HREM micrographs

Lattice strain was been estimated both manually from HRTEM images, and from the SAED patterns using GPA analysis. The basis of the GPA method is described in detail by Hÿtch, et al. [24]. Briefly, the phase component of an image in complex space provides information about local lattice displacements and distortions in a direction normal to the lattice fringes corresponding to the position of the Bragg spot. GPA therefore involves filtering a HRTEM micrograph with an asymmetric filter centred on a Bragg spot in the Fast Fourier transform (FFT) of a HRTEM micrograph and then performing an inverse Fast Fourier transform (IFFT). Subsequently, by derivation of the calculated displacement from two non-collinear Fourier components, the local strain fields are generated, wherein the local strain tensor at each atomic fringe position may be constructed. In this way, regions of the material with different levels of strain may be identified. Geometric Phase Analysis (GPA) was conducted using the established open-source software package Strain+ + [24], which is specifically planned for quantifying lattice strain and distortion from high-resolution transmission electron microscopy (HRTEM) imaging. This permits the strain fields to be visualized using various tools, such as contour- or heat-maps.

The basis of GPA [24] is the comparison of the phase of a set of perfect planes (defined by a *g*-vector) to the planes measured from an image (defined by a mask at the *g*-vector). The geometric phase $P_g(r)$ of the local Fourier components is directly related to the components of the displacement field, $u(r)$, in the direction of the reciprocal lattice vector g. $P_g(r)$ is given by:

$$P_g\,(r) = -2\pi g.u(r) \tag{1}$$

To generate the full strain field, the phase should be estimated for two non-collinear *g*-vectors, wherein both phases are related by the value, u, which defines the displacement field. The 2-dimensional displacement field can be determined by measuring two phase images, $P_{g1}(r)$ and $P_{g2}(r)$:

$$u(r) = -\frac{1}{2\pi}[P_{g1}(r)a_1 + P_{g2}(r)a_2] \tag{2}$$

where a_1 and a_2 are the lattice vectors in real space corresponding to the reciprocal lattice vectors defined by g_1 and g_2, respectively. The 2-dimensional displacement field is then written as:

$$\begin{pmatrix} u_x \\ u_y \end{pmatrix} = -\frac{1}{2\pi}\begin{pmatrix} a_{1x} & a_{2x} \\ a_{1y} & a_{2y} \end{pmatrix}\begin{pmatrix} P_{g1} \\ P_{g2} \end{pmatrix} \tag{3}$$

wherein, the components of the plane strain, ε, are given by:

$$\varepsilon_{xx} = \frac{\partial u_x}{\partial x}$$

$$\varepsilon_{yy} = \frac{\partial u_y}{\partial y}$$

$$\varepsilon_{xy} = \varepsilon_{yx} = \frac{1}{2\pi}\left(\frac{\partial u_x}{\partial y} + \frac{\partial u_y}{\partial x}\right) \tag{4}$$

2.4. Strain mapping using strain+ + software

The GPA theory described above was implemented in this work using the open-source software Strain+ +. From the TEM image, an example of which is shown in Fig. 1(a), the corresponding FFT pattern, as shown in Fig. 1(b), is generated, where for the purpose of illustration we have used the micrograph from the 150–106 μm drop-tube sample. By virtue of the FFT, periodicity in the spatial domain, encode by pixel intensities within the HRTEM image, are transformed into complex numbers containing both magnitude and phase information in the frequency domain. We then select two spots that will correspond to the g_1 and g_2 vectors, in this case $g_1 = 1\bar{1}\bar{1}$ and $g_2 = 0\bar{2}\bar{2}$. Comparison of the g_1 and g_2 vectors in the frequency domain allows the shift in atomic positions relative to the ideal lattice, i.e. the lattice strain, to be determined. An inverse FFT (iFFT) allows this information to be displayed in the spatial domain.

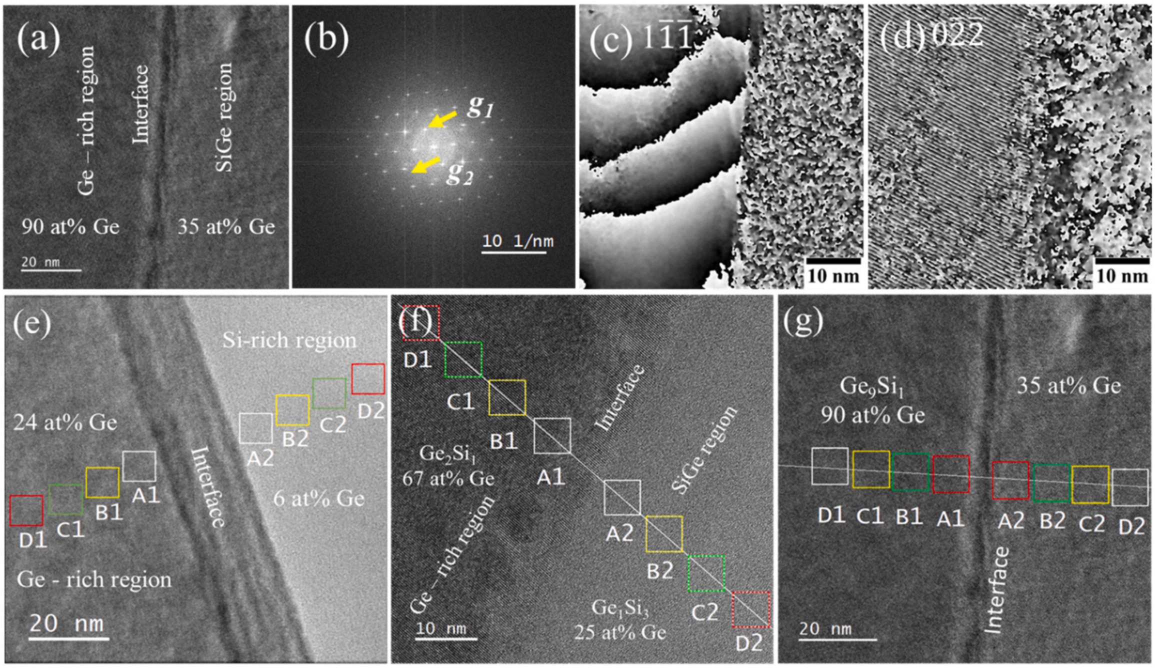

Fig. 1. a) High-resolution transmission electron microscopy (HRTEM) image across a step-mediate concentration jump in the 150–106 µm drop-tube material, b) Fast Fourier transform (FFT) pattern of the HRTEM image, with reference lattice spots for the $g_1 = 1\overline{1}\overline{1}$ and $g_2 = 0\overline{2}\overline{2}$ vectors, c) normalised $1\overline{1}\overline{1}$ and d) normalised $0\overline{2}\overline{2}$ phase images, as obtained using the Strain+ + software from the HRTEM micrograph shown in Fig. 1(a), and HRTEM images of step-mediated concentration jumps in e) crucible residual, f) rapidly solidified > 850-µm and g) 150–106-µm drop-tube samples, showing locations A1-D1 and A2-D2 normal to interface used for manual lattice distortion measurement.

Example phase map output from Strain+ + is shown in Fig. 1(c) & (d). Here, a transition from black through to white corresponds to a phase shift from -π to + π, i.e. the phase difference between one (say) black fringe to the next black fringe is a phase shift of 2π, corresponding to a displacement of one atomic lattice spacing, a. Such phase maps may then be converted to strain maps, giving the ε_{xx}, ε_{yy} and $\varepsilon_{xy} = \varepsilon_{yx}$ components of the strain.

Such an analysis has been undertaken for all three TEM samples (crucible residue, >850-µm and 150–106-µm drop-tube samples). The Strain+ + masks used were $g_1 = \overline{2}00$ and $g_2 = \overline{13}1$ for the crucible residue and $g_1 = \overline{1}11$ and $g_2 = 113$ for the > 850-µm drop-tube sample. The phase maps for these two materials (crucible residue and >850-µm drop-tube samples) are shown in supplementary information, Figure S3 and Figure S4, respectively.

2.5. Manual lattice determination

In addition to the GPA strain mapping undertaken using Strain+ +, manual lattice strain determination has also been undertaken. For each sample one interface marking a concentration step has been identified and four small, co-linear regions lying along the normal to the interface have been identified on either side of the interface, as shown in Fig. 1(e-g) for the three samples in question. High resolution iFFT images have then been obtained, wherein lattice fringes are evident and the average lattice spacing, a, within each region, together with their orientation with respect to the interface can be determined directly. An example iFFT image, together with a plot of the fringe intensity along the line shown, is given in supplementary information, Figure S5. Using such intensity plots, the average lattice spacing, typically averaged over 12–18 fringes, is obtained for each region.

In order to convert the measured lattice spacing into an equivalent strain, the nominal lattice spacing, a_0, is required, wherein the strain ($= \frac{\Delta a}{a_0} = \frac{a - a_0}{a_0}$) may be determined. For the six areas considered here (three samples, 2 sides of an interface with different concentrations in each case) the concentration is known precisely from TEM EDX analysis. a_0 is then constructed from Vegard's law using the determined compositions with $a_{Si} = 0.543102$ nm and $a_{Ge} = 0.561619$ nm. The validity of Vegard's law as applied to Si-Ge has been evaluated, albeit in thin films, by Kasper, et al. [25]. In re-evaluating their data, we find that the root-mean-square (RMS) deviation from Vegard's law in the composition interval studied by these authors (9.7–70.8 at% Ge) is < 0.02%. Moving from a linear (Vegard's law) to quadratic fit between composition and lattice parameter reduces the RMS residual to < 0.01%, but given that both film thickness and the strain state of the film varied between samples in the experiments of Kasper, et al. [25], we see little reason to move to a more complex relationship and take Vegard's law as being valid for Si-Ge.

3. Results and discussion

According to the model of by Oloyede, et al. [22], the calculated cooling rates for the undercooled liquid of the > 850 and 150–106 µm SiGe droplets sizes is 1425 and 27500 K s^{-1} respectively. The cooling rate of the residual material (0.172 K s^{-1}, or 10 K min^{-1}) was known precisely because of the controlled cooling of the drop-tube furnace following ejection.

Example bright-field TEM micrographs from the 150–106-µm sample are shown in Fig. 2(a), wherein several clear step changes in the contrast are displayed within the microstructure. High-Z regions appear darker, while low-Z regions appear brighter. From Fig. 2(a), we observe that one of the large very Si-rich grains (Region 1, bright phase) is located on the left-hand side of the micrograph, with the transition into the intermediate Ge-rich grain boundary defined by a clear change in contrast. Another stepped contrast transition may be observed towards the very Ge-rich grain boundary (Region 4, dark phase). A further contrast step change may also be observed towards the right-hand margin of the micrograph, wherein the transition into another intermediate Ge-rich phase is observed. Fig. 2(b) provides a magnified view of Interface 1 (between the Ge-rich region (Region 4) of 90 at% Ge and the SiGe region

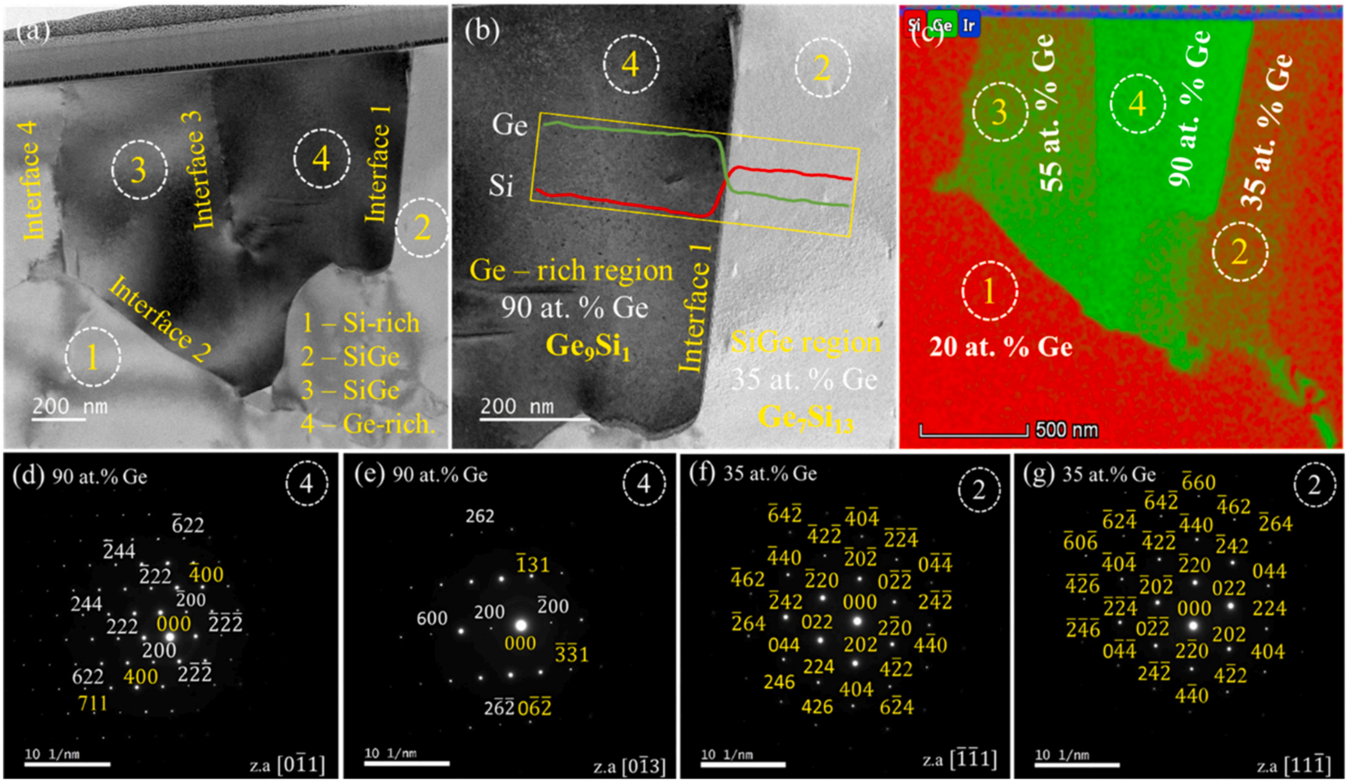

Fig. 2. (a) Bright-field TEM image of the 150–106 μm drop-tube material, showing contrast differences between high-Z (Ge-rich) and low-Z (Si-rich) regions, (b) Magnified view of Interface 1 with EDX line scan superimposed to show composition uniformity, (c) Corresponding EDX map with numbered regions; detailed compositions are described in the text. [Note: The Si-rich region is that at the grain boundary, which is still more Ge-rich than the Si-rich bulk grains, and SAED patterns taken from: d) & e) 90 at% Ge region shown in Fig. 2(b) with zone axes $[0\bar{1}1]$ and $[0\bar{1}3]$ respectively; f) & g) 35 at% Ge region shown in Fig. 2(b) zone axes $[\bar{1}\bar{1}1]$ and $[11\bar{1}]$ respectively. Allowed reflections for the diamond cubic structure are shown in yellow, while forbidden (i.e. superlattice) reflections are shown in white. For panels (d) and (e), the reflections density is sufficiently high that only selected reflections are labelled for clarity. Indexing has been assigned to all visible reflections, even if not all are labelled in the figure.

(Region 2) of 35 at% Ge), with the EDX line scan superimposed to illustrate the uniformity of composition within the two regions. To establish the formation of fixed stoichiometries in these regions, the compositions within each region are constant and are measured at 90 at % Ge (Ge_9Si_1) and 35 at% Ge (Ge_7Si_{13}), respectively, with a near atomically sharp transition between them. The corresponding EDX map (Fig. 2(c)) provides a clearer indication of the step-change nature in concentration at all of the boundaries (Iridium observed at the top of the micrograph has been used as a protective layer in order to shield the sample during FIB milling). As such, four distinct regions are identified: Region 1 – 20 at% Ge (Si-rich), Region 2 – 35 at% Ge (SiGe), Region 3 – 55 at% Ge (SiGe), and Region 4 – 90 at% Ge (Ge-rich). Similar, if less extreme compositional step-changes are also observed in the crucible residue (24 at% Ge with step change to 6 at% Ge) and > 850-μm samples (67 at% Ge with step change to 25 at% Ge) (see panel (a) in Figure S6 and Figure S7), consistent with previous works [4,7,23] that the material becomes more heterogeneous as the cooling rate increases.

Discrete, stepwise enrichment of Ge toward the grain boundaries is observed in the 150–106 μm droplet and is also evident in additional examples reported by Al-Jenabi, et al. [7], and Al-Jenabi [23], where TEM/EDX line scans demonstrate stepwise segregation of Ge rather than the continuous enrichment expected from the equilibrium phase diagram, illustrating the step-mediated partitioning during solidification.

Henceforth, we will refer to this type of structure as step-mediated partitioning, this being a solidification induced effect in which compositional changes resulting from partitioning of solute during solidification occur in discrete, atomically sharp steps, with each step giving a distinct local composition which then remains constant over a spatially extended region of the solid before the composition changes again at another such atomically sharp step. The result in the as-solidified product is that within a region where the Ge concentration is changing, this does so via a number of discrete steps between regions of constant composition. This is contrary to the smooth, continuous compositional gradients predicted by Scheil type partitioning based upon the Si–Ge phase diagram. Unlike the work of Taniguchi, et al. [26], we do not observe nanoscale Ge-rich precipitate formation at the Si/SiGe interfaces. Such precipitate formation may therefore be a consequence of either the magnetron sputtering technique employed by Taniguchi, et al. or the very narrow confinement produced by alternating nanometre scale layers.

Such step-mediated partitioning is highly unusual for a system with an isomorphous phase diagram. Among metallic isomorphous alloys, Ni–Cu is the most extensively studied system and represents the clearest analogue to Si–Ge. Despite the large body of work on Ni–Cu, including rapid solidification studies, no evidence has been reported of step-mediated partitioning or anomalous chemical heterogeneity [27–29]. The Au–Ag system is also isomorphous but behaves as an almost ideal solution, with an extremely narrow solidus–liquidus gap and negligible enthalpy of mixing, making kinetic segregation unlikely. Existing results are consistent with the behaviour of Ni–Cu, although experimental studies are complicated by the volatility of silver [30]. The Au–Cu system, by contrast, undergoes a disorder–order transformations at low temperature. Recent work on Cu–56 at% Au demonstrates that ordering at 250 °C is extremely sluggish, requiring extended annealing to reach completion, and proceeds even more slowly in plastically deformed samples [31]. Such behaviour confirms the tendency of Au–Cu alloy to form ordered compounds, but these transformations are associated with solid state annealing processing, and no evidence of step-mediated partitioning has been observed. As such, these comparisons reinforce that the anomalous chemical partitioning observed in Si–Ge are peculiar to covalently bonded semiconductors and not reproduced in classical metallic isomorphous alloys.

The volume fraction of the Ge-rich regions has previously been determined from normalised SEM–BSE images using Otsu thresholding, validated by SEM–EDX Ge maps [7]. At SEM resolution, all Ge-enriched regions appear as a single, continuous bright network and are grouped into a single Ge-rich category. TEM–EDX mapping of site-specific FIB lamellae shows that this SEM-defined Ge-rich regions can be subdivided into multiple distinct compositional sub-regions, each with relatively uniform Ge content and separated by atomically sharp interfaces. Four such regions are identified in Fig. 2(c), with other samples showing different compositional regions. The volume fractions of the Ge-rich regions, measured by SEM–BSE thresholding across the whole range of drop-tube powders synthesised range from 20.8 ± 0.43% for the > 850 μm droplets to 11.8 ± 0.72% for 53–75 μm droplets, albeit this latter has not been subject to the detailed TEM analysis reported here. For reference, for the 150–106 μm droplets that have been subject to detailed TEM analysis, the value is 12.41 ± 0.44%, while for the starting material this is 37.2 ± 2.6% [7]. These values are statistically representative of the bulk material and exhibit a systematic decrease with increasing cooling rate, the decreasing volume fraction being balanced by higher Ge concentrations in these regions. These values are therefore used in preference to TEM-based measurements, which would be biased by the exceptionally small, targeted, sampling area used in TEM studies.

SAED patterns have been taken from multiple regions in all three samples, with the focus being upon obtaining patterns from adjacent regions on either side of a step mediated concentration jump. Fig. 2 shows two representative examples of such, obtained from the regions displaying compositions of 35 at% Ge and 90 at% Ge as shown in Fig. 2 (b), with the diffraction results for the high-Ge material being shown in panels (d & e) of the figure and that for the low-Ge material in panels (f & g). Indexing of the diffraction patterns was performed off-line using the Single Crystal software package. During SAED pattern acquisition from adjacent regions of different composition, the sample orientation was held as near to constant as possible, within the requirements of obtaining well-formed diffraction patterns. We note that this has resulted in the SAED patterns shown in Fig. 2 displaying different zone axes, in some cases with large angles between the stated zone axis directions. Given that all sample areas were within a 500 nm radius, this likely reflects actual variability within the sample. Indeed, this appears to be an inherent feature of these materials, with all three samples consistently displaying this tendency.

As shown in Fig. 2(f & g) all diffraction spots for the low-Ge material (with indexing shown in yellow), correspond to allowed reflections in the diamond cubic crystal structure appropriate to Si-Ge alloy. Conversely, in the high-Ge material (Fig. 2d & e), many of the diffraction

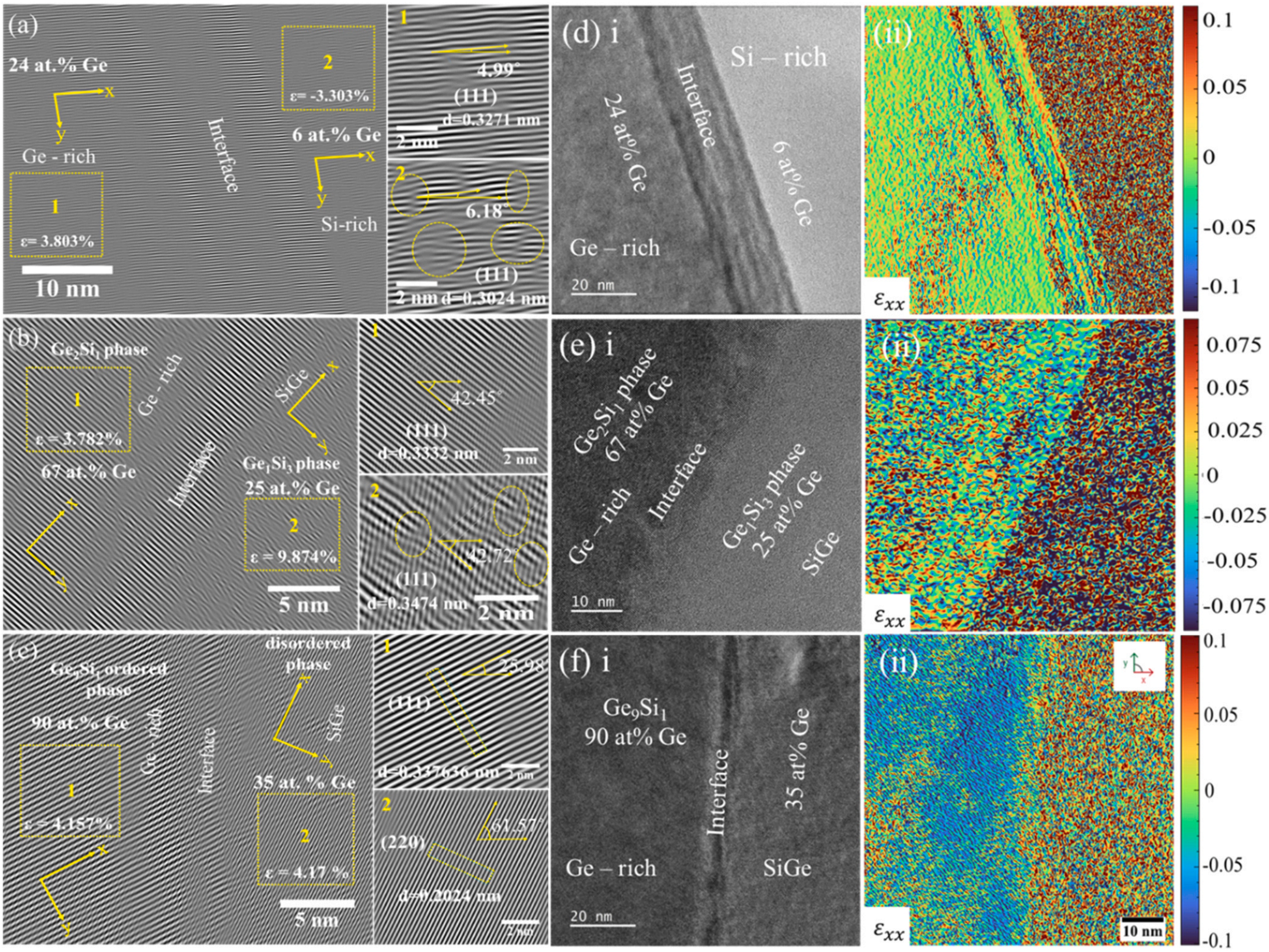

Fig. 3. Left: Inverse Fast Fourier transform (IFFT) image in the vicinity of a step-mediated concentration jump from HRTEM of a) residual, b) rapidly solidified > 850-μm and c) 150–106-μm drop-tube samples, in each case showing the calculated lattice *d*-spacing, angle between the lattice fringes and the horizontal and selected dislocations (circled in yellow); Right: HRTEM micrographs (i) and the corresponding strain maps (ii) showing the strain component ε_{xx} generated by Strain+ + for (d) residual, (e) rapidly solidified > 850-μm, and (f) 150–106-μm samples.

spots are along forbidden directions for the diamond cubic structure, as indeed are the zone axis directions. Here, due to the density of spots, we have not included the indexing for the allowed reflections (in Fig. 2(d) & e, only 3 allowed reflections be labelled in yellow for distinction), but have instead only included (in white) indexing for reflections that should be disallowed within the diamond cubic crystal system, i.e. the labelled spots in white are superlattice reflections and as such provide clear evidence for chemical ordering within the more Ge-rich material. This trend is consistently repeated in the other two samples. In both the crucible residue and > 850-μm drop-tube sample, superlattice spots were observed in the Ge-rich grain boundaries but not in the Ge-deficient regions. SAED patterns for these two materials (crucible residue and >850-μm drop-tube samples) are shown in supplementary information, Figure S6 and Figure S7, respectively.

High Resolution TEM (iFFT) micrographs for an interface displaying a step change in concentration for each of the three samples considered here are shown in Fig. 3. In panel (a) of the figure we have the interface between Si-6 at% Ge and Si-24 at% Ge regions in the slowly cooled crucible residue material, in panel (b) the interface between the Si-25 at % Ge and Si-67 at% Ge regions in the > 850-μm drop-tube sample (estimated cooling rate 1425 K s^{-1}) and in panel (c) the interface between the Si-35 at% Ge and Si-90 at% Ge regions in the 150–160 μm sample (estimated cooling rate 27500 K s^{-1}). The location of the interface is not clear from the fringe pattern in any of the images and consequently has been indicated in the main panel of each figure, with this location being identified from the EDX composition boundary. Also shown in the main panel of each figure are the *x* and *y* directions defined parallel and perpendicular to the fringes respectively, these being the directions used for strain determination. A small region on each side of the interface is shown in more detail to the right of each main figure, with the region selected being indicated by the yellow box. In the detailed images to the right we also show the planes being imaged, a manual determination of the inclination of the fringe direction to the notional horizontal on the image and the determined avaerge *d* spaging for the fringes.

The interfaces for the crucible residue and > 850-μm drop-tube samples are generally as we might expect, falling into the coherent or semi-coherent classification. The fringe orientation is (111) on both sides of the interface with fringes that are continuous across the interface. In both cases there is a small change in lattice parameter across the interface, with $d_{(111)}$ changing from 0.3024 nm to 0.3271 nm (a = 0.5238 nm to a = 0.5666 nm) moving from low to high Ge in the crucible residue and $d_{(111)}$ changing from 0.3474 nm to 0.3332 nm (a = 0.6017 nm to a = 0.5771 nm) moving from low to high Ge in the > 850-μm drop-tube sample. These correspond to 7.9% and −4.2% changes in lattice spacing in the two samples respectively, where the strain across the interface is defined as:

$$\varepsilon = \frac{2(a_{\mathrm{High\_Ge}} - a_{\mathrm{Low\_Ge}})}{(a_{\mathrm{High\_Ge}} + a_{\mathrm{Low\_Ge}})} \tag{5}$$

so as to not make any assumptions about what the lattice spacing should be and with *a* being determined in the A1 and A2 positions so as to be as close as possible to the interface. By comparison, the expected strain across the interface, for a system exactly obeying Vegard's law, and displaying the concentration jumps characteristic of these two specimens would be 0.78% and 1.8% for the crucible residue and > 850-μm samples respectively.

Examination of panels (a) & (b) of Fig. 3 show a high density of dislocations, with these being concentrated mainly on the Ge-deficient side of the interface, with some such being circled in the inset images to the right of the main HRTEM micrographs. This is consistent with our description of these interfaces as being semi-coherent. Visually, the density of dislocations appears to be somewhat higher for the > 850-μm drop-tube sample than for the crucible residue, which would be consistent with somewhat larger step change in composition across the interface in this sample. As an aside, we note that the high density of dislocations on the Si-rich side of the interfaces makes accurate determination of the lattice spacing difficult, as this is subject to change in the vicinity of the dislocation. This may explain the anomalous negative strain across the interface for the > 850-μm drop-tube sample, which itself arises from an anomalously high value of *a* on the Si-rich side of the interface, a = 0.6017 nm being higher than that for either Si or Ge (wherein such a value cannot be fitted from a simple application of Vegard's law). However, even if we take an average of the lattice spacings across the four locations A-D on either side of the interface we still obtain a negative value for the strain

In constrast to the semi-coherent interfaces observed in Fig. 3(a & b), the image in Fig. 3(c) for the 150–106 μm sample appears to be that of an incoherent interface, with (111) planes visible on the Ge-rich side of the interface and (220) planes visible on the Si-rich side of the interface. That said, the interface does not resemble a typical incoherent interface as we might expect of say a precipitate within a matrix of a different material. The interface exhibits a predominantly coherent nature within the immediate interface region, as evidenced by the continuous presence of (111) planes extending from the 90 at% Ge regions across the interface. In particular, in the absence of composition mapping it would be difficult to identify the location of the interface on the basis of its crystallographic features. Nevertheless, this coherence diminishes within the next 5–7 nm, resulting in a discernible shift in orientation approximately 10 nm away from the interface (specifically, at the right-hand margin of the image), where a notable transition to a (220) orientation predominates. It is noteworthy that 10 nm is very large within the context of atomic interfaces, given that typically, transitions between distinct crystallographic arrangements occur over a much shorter distance, typically 3–5 at. diameters, even in the case of an atomically rough interface. We also note that, unlike the micrographs shown in Fig. 3(a & b), there is almost no evidence of dislocations in Fig. 3(c). The corresponding *d* spacings are $d_{(111)} = 0.3376$ nm (a = 0.5847 nm) on the Ge-rich side of the interface and $d_{(220)} = 0.2024$ nm (a = 0.5724 nm) on the Si-rich side of the interface. This corresponds to a stain, calculated using Equ. (5) of 2.1%, compared with an expectation from Vegard's law for a 55% Ge-concentration step (from 35 at% Ge to 90 at% Ge) of 2.3%. This result therefore seem curious, in that we have a smaller latiice mismatch in the sample displaying an apparently incoherent interface than in either of those displaying a semi-coherent interface.

In order to shed further light on this seemingly anomalous result we consider the measured angular mismatch between the lattice planes on either side of the interface in each of the three samples, using the orientation angles annotated onto Fig. 3(a-c). For the crucible residue and > 850-μm drop-tube samples these are 1.2° and 0.3° respectively. For these samples, which display the same crystallographic orientation on either side of the interface, these differences presumably arise from measurement error, particularly on the more Si-rich side of the interface, where the high density of dislocations means that the lattice fringes are not always perfectly parallel. In contrast, in the 150–106-μm sample the angle between the (111) lattice planes on the Ge-rich side of the interface and the (220) planes on the Ge-deficient side of the interface is 35.6°. Interestingly, the expected angle, θ, between (111) and (220) planes, given by:

$$\cos\theta = \frac{h_1h_2 + k_1k_2 + l_1l_2}{\sqrt{({h_1}^2 + {k_1}^2 + {l_1}^2)({h_2}^2 + {k_2}^2 + {l_2}^2)}} \tag{6}$$

assuming a common underlying crystallography, is 35.3°, wherein such an assumption of a common underlying crystallography would appear justified. Consequently, rather than an incoherent interface in Fig. 3(c), what we appear to have an interface at which there has been a change in the growth direction but where the underlying unit cell has been preserved.

The results of performing GPA strain mapping using Strain+ + on the three samples in question are shown in Fig. 3(d-f), together with, in each case, a bright field TEM image of the same area so that the interface region can be located independent of the strain maps. As described in the Methodology section, GPA analysis produces three independent strain-fields ε_{xx}, ε_{yy} and $\varepsilon_{xy}(=\varepsilon_{yx})$. However, due to the high degree of qualitative similarity between the three maps for each of the samples considered here, and for the sake of brevity, in Fig. 3d-f(ii) we display only ε_{xx}. The full set of maps are available in the supplementary information (Figure S8). As with the HRTEM images there are distinct similarities in behaviour for the crucible residue and $>$ 850-μm drop-tube samples, shown in Fig. 3(d and e). On the Ge-rich side of the interface the strain is relatively uniform and close to zero, albeit with rather more local variation for the $>$ 850-μm drop-tube sample, while on the Si-rich side of the interface both samples show very short wavelength variations in strain between a maximum and minimum values (approximately $\pm$ 0.1 for the crucible residual and $\pm$ 0.075 for the >850-μm drop-tube sample), giving rise to a 'speckle' pattern. Conversely, when we look at the 150–106 μm sample (Fig. 3f), distinct differences may be observed. In particular, although large areas on the Ge-rich side of the interface still display a near uniform strain, particularly in the interface region, this uniform strain is now close to the minimum value of -0.1. However, on the Si-rich side of the interface we still have a speckle pattern, with short wavelength variation between the maximum and minimum values of $+$ 0.1 and -0.1 respectively. In all three cases the average strain within the speckle pattern regions is small but positive, typically of the order 0.02.

GPA, as applied here, is capable of quantifying interfacial strain fields with sub-percent sensitivity (roughly 0.05–0.1%) and nanometre-scale spatial resolution [24,32–34], making it particularly well suited for the analysis of the highly localised distortions observed at step-mediated compositional interfaces. The extrema observed here, up to ±0.1 in ε_{xx} in the crucible residue sample, and ±0.075 in the $>$ 850 μm drop-tube sample, may be contrasted with fracture strains for bulk silicon which are much lower, typically ~0.1–0.2% (in tension [35]). Thin-film polysilicon used in micro-electromechanical systems (MEMS) devices, can however reach 0.5–2.0% before fracture, owing to reduced flaw sizes and optimised processing [36,37]. The very high values of ε observed here should however be interpreted not as bulk elastic strains, but as highly localised lattice distortions concentrated near step-mediated compositional interfaces. These interfaces frequently exhibit high dislocation densities, abrupt concentration gradients, and interfacial ordering, all of which contribute to strain concentrations detectable via GPA. We also admit the possibility that the near constant value of $\varepsilon_{xx} = -0.1$ in the 150–106 μm drop-tube sample might be an artefact of the change in growth direction identified in Fig. 3(f)(ii), with the change in growth direction mistakenly being identified as a large strain. Manual lattice-spacing measurements across such interfaces yield more moderate values (3.44–4.79%), consistent with Vegard's law and expected solid-state behaviour. Consequently, although the local maxima exceed typical values reported in Si/SiGe heterostructures ($\leq$ 1–2%) [32,34], we believe they remain physically reasonable at the nanoscale and should not result in macroscopic yield. In this respect we note that silicon nanowires and whiskers can sustain purely elastic strains of 10–17% displaying tensile strengths of 10–20 GPa [38,39], consistent with *ab initio* predictions for the ideal strength of silicon [40].

To supplement the GPA strain mapping using Strain+ +, we have also undertaken manual strain determinations for all three samples. In each case we have taken a transect normal to the interface and selected 4 sampling regions on either side of the interface, with those on the more Ge-rich side of the interface being denoted by A1-D1 and those on the Ge-deficient side of the interface being denoted A2-D2. On both sides of each interface A is closest to the interface and D furthest from it. The locations of these sampling regions are shown in Fig. 1(e-g).

The degree of lattice distortion is expressed as the change in lattice spacing via the equation $\Delta a/a_0 = (a - a_0)/a_0 \times 100\%$, where a is the measured lattice parameter and a_0 its nominal value estimated from Vegard's law, with the compositions as determined from TEM-EDX data. Inherent within this is the assumption that the lattice parameters calculated using Vegard's law are appropriate and, in particular that chemical ordering does not result in a change in lattice parameter relative to that for a random solid-solution. However, we also note that while the absolute values of the lattice distortion would thus be affected if chemical ordering were to so affect the lattice parameter, the trends moving along each transect are likely to remain valid. The lattice distortion values calculated for each sample are given in Table 1.

A number of trends can be discerned from Table 1 notably that, for all three samples, there is considerably more local variability in the lattice strain on the Ge-deficient side of the interface than on the Ge-rich side. This is particularly the case for the residual and $>$ 850 μm drop-tube samples, where the range in the data on the Ge-deficient side of the interface is 13.74% (between C2 and D2) for the residual and 5.22% (between B2 and C2) for the $>$ 850 μm drop-tube sample. This is consistent both with the GPA strain mapping, which shows strong, short wavelength, local variations in the strain field in the Ge-deficient material, and with the HRTEM images which show that the Ge-deficient regions of these samples display a high density of dislocations. Such a high density of dislocation would give rise to such variability in the measured lattice spacing. The range in the values on the Ge-deficient side of the 150–106-μm sample is rather smaller at 1.24% (between A2 and D2), reflecting the much lower density of dislocations mediated by the change in growth direction in this material.

In contrast, we see much less variability in lattice spacing on the Ge-rich side of the interface in the three samples. Again, this is consistent with both the HRTEM images which show a much lower density of dislocations on the Ge-rich side of the interfaces and with the GPA analysis, which indicates near uniform strain on the Ge-rich side of each interface. The average strains recorded on the Ge-rich side of the interface are 3.49%, 3.44% and 4.79% for the crucible residue, $>$ 850-μm and 150–106-μm drop-tube samples respectively. This is consistent with the GPA strain maps which show a more uniform strain distribution on the Ge-rich side of each interface, and which show similar and uniform strain fields for the crucible residue and $>$ 850-μm drop-tube samples and a more strained, but still relatively uniform, strain field in the 150–106-μm drop-tube sample.

The solidification sequence, were the Si-14.2 at% Ge alloy to follow the equilibrium phase diagram, is straightforward. From the phase diagram the equilibrium partition coefficient at 14.2 at% Ge is $k_E = 0.416$ wherein, assuming negligible undercooling, the initial solid to form would be Ge-deficient with a concentration of 5.9 at% Ge. As solidification proceeds k_E decreases further resulting in an increasingly Ge-rich residual liquid. A Scheil calculation by Hussain, et al. [4] demonstrated that in this scenario the Ge concentration of the residual liquid increases throughout solidification, with the final liquid to solidify being essentially pure Ge. At the coarsest level, this is indeed what we observe, with large Ge-deficient grains and grain boundary regions significantly enriched in Ge. This may explain why the unusual behaviour observed here has not been more widely reported. However, our initial observation differs significantly from this prediction in one key respect. Based upon the equilibrium phase diagram we would expect the Ge concentration to increase in a continuous manner as we transverse the grain boundary, but this is not the case. Instead, we see regions of constant concentration, followed by a discrete step to a higher concentration that itself is then constant over a certain distance. That is, we observe a step-mediated concentration profile. Moreover, these discrete compositions tend to be multiples of 5 at%, with compositions of 5, 20, 25, 65, 70 and 85 at% Ge all being observed. As an aside we note that such compositions, which are multiples of 5 at%, do not naturally correspond to chemical ordering of the 8 atoms on the standard diamond cubic unit cell, suggesting that there may be some super-cellular ordering occurring. Interestingly, Németh, et. al. [41] have found evidence for 5-fold ordering in diamond, wherein an ordered super-cell comprising 5 diamond cubic unit cells would admit discrete compositions with 5 at%

Table 1
Manual lattice distortions measurements for selected locations normal to interface shown in Fig. 1(e-g).

Location	a_{SiGe} (HRTEM) nm	Lattice distortion %	a_{SiGe} (HRTEM) nm	Lattice distortion %	a_{SiGe} (HRTEM) nm	Lattice distortion %
	Residue sample 24 at%Ge, $a_0 = 0.5475$ nm 6 at% Ge, $a_0 = 0.5442$ nm		$>$ 850-µm sample 67 at% Ge, $a_0 = 0.5555$ nm 25 at% Ge, $a_0 = 0.5477$ nm		150–106-µm sample 90 at% Ge, $a_0 = 0.5598$ nm 35 at% Ge, $a_0 = 0.5496$ nm	
A1	0.5666	3.48	0.5772	3.90	0.5852	4.55
B1	0.5658	3.33	0.5768	3.83	0.5844	4.39
C1	0.5659	3.35	0.5700	2.62	0.5844	4.40
D1	0.5683	3.79	0.5746	3.44	0.5830	4.14
A2	0.5238	-3.74	0.6018	9.86	0.5724	4.16
B2	0.5585	2.62	0.6019	9.89	0.5768	4.95
C2	0.5983	9.94	0.5733	4.67	0.5751	4.64
D2	0.5235	-3.80	0.5851	6.82	0.5793	5.40

increments (and indeed 2.5 at% increments). However, we also note that although the compositions are multiples of 5 at%, the composition step changes observed are often $> >$ 5 at%, with for instance a jump from 20 at% to 65 at% Ge being observed in the $d >$ 850-µm drop-tube sample, despite intermediate compositions being observed elsewhere.

However, this is not the only respect in which this alloy shows unexpected partitioning behaviour. Virtually all simple alloys show improved chemical homogeneity under rapid solidification conditions due to the action of kinetic solute trapping, models for which are described by Aziz [42], Sobolev [43] and Galenko [44]. Based upon estimates by Mullis, et al. [45] and by Nan and Bing-Bo [46], drop-tube samples of high-melting-point materials with size fraction of 150–106 µm are expected to achieve an undercooling in the range 250–300 K. The data of Panofen and Herlach [47] for Si-10 at% Ge (Si-22.3 wt% Ge), indicate that this should contribute to a growth velocity of around 10 m s^{-1}.

Notwithstanding the above findings that the material becomes more heterogeneous under rapid solidification conditions, rather than less, there maybe some evidence for solute trapping in the large Si-rich primary grains. Compositional measurements reported in Ref. [23] indicate a modest upward trend with decreasing particle size, increasing from ~14 wt% Ge under equilibrium conditions, to a plateau of ~17.5 wt% Ge in the smaller size fractions. Such behaviour maybe consistent with the onset of solute trapping at growth velocities of approximately 7–8 m s^{-1}. The data would be compatible with the measurement of solidification velocity in various Si-Ge alloys by Panofen and Herlach [47], with most such alloys displaying a plateau in growth velocity with increasing undercooling. However, we note that the extent of solute trapping, if present, in Si-Ge appears more restricted than in many other systesms and that similarly, the onset velocity is high relative to other systems. Pulsed laser melting experiments on Si-Ge Brunco, et al. [48] have previously been used to determine a diffusive speed for Ge in Si of around 2.5 m s^{-1}, which does not appear consistent with the results of either Panofen and Herlach [47] or Al-Jenabi [23], wherein we cannot therefore rule out that the step-mediated partitioning mechanism also plays a role in inhibiting solute trapping.

We also note that in a number of the more Ge-rich regions within our samples, clear evidence of chemical ordering is present in the form of superlattice spots observed in SAED patterns. Again, this behaviour is contrary to that expected from the equilibrium phase diagram, which is of the isomorphous form with a single phase random solid solution occupying the whole composition range. Interestingly, such chemical ordering is seen in even the most rapidly solidified samples where, as with solute trapping, we would expect disorder trapping [49,50] to mediate a transformation from ordered to disordered structures once the growth velocity exceeded the diffusive speed in the material. However, that ordering is observed predominantly in the interdendritic regions, which solidify last and therefore at relatively slow local growth velocities during the post-recalescence phase of solidification. In contrast, the primary Si dendrites, formed during the high-velocity recalescence phase of solidification, exhibit a disordered structure, which may be consistent with disorder trapping if there is a tendency for both phases to order. Comparable behaviour has been reported in β-Ni_3Ge by Mullis and Haque [51], where selective etching revealed that high-velocity growth during recalescence produced disordered dendrites embedded within an ordered matrix of what was otherwise the same phase, formed from the residual liquid during slower post-recalescence solidification. In both systems, the slower growth of the interdendritic regions permits sufficient atomic mobility for ordering to develop despite the overall rapid cooling rate.

However, while the observed behaviour is unusal in terms of the bulk material, there are paralells for this behaviour in Si-Ge thin films with papers by Araki, et al. [19] and Müllers, et al. [20] reporting step-mediated concentraion gradients in such films. Moreover, chemical ordering appears to be intrinsically linked to the occurance of step-mediated concentration gradients, with Muller *et al.* identifying two possible ordered Si-Ge structures (which they refer to as RS1 and RS2, where RS stands for rhombohedral structure) while Araki, et al. [19] identify 3 (which they term RH1/1, RH2/2 and RH2/1, where RH denotes rhombohedral configuration). Indeed, Araki, et al. [19] assert that step-mediated concentration gradients necessarily require the material on at least one side of the step interface be chemically ordered.

In both studies the key point is that the large lattice mismatch between Si and Ge (typically reported as 4.24%) results in considerable lattice strain in a random solid solution, with strain energy calculations by Araki, et al. [19] indicating that strain enhanced diffusion can promote the formation of chemically ordered structure combined with step-mediated concentration gradients as a mechanism for the minimisation of this lattice strain. In particular, certain ordered structures can minimise the elastic strain energy, with Araki's RH2/1 and Muller's RS1 structures being identified in this context. The key here appears to be minimising the number of Ge-Ge (large atom-large atom) bonds with, for instance, at a notional 50:50 Si:Ge stoichoimetry, the RH2/1 structure having 16% Ge-Ge bonds compared to 19% in RH1/1 and 26% in RH2/2. Consequently, although the studies described above relate specifically to thin films and not to bulk samples solidified from their parent melt, they certainly provide a motivation for investigating the lattice strain on either side of a step-mediated concentration interface in our bulk Si-Ge samples.

For the two more slowly cooled samples (crucible residue and >850-µm drop-tube sample), the HRTEM micrographs display a semi-coherent interface across the step-mediated concentration jump which is relatively diffuse, to the point that it is difficult to identify the exect location of the interface from the micrograph, despite this appearing near atomically sharp in the EDX maps. However, despite this, a sharp interface between the Si-rich and Ge-rich material is delineated in the GPA strain mapping derived from the HRTEM images. Numerous dislocations are visible in the micrographs, with these appearing to be located almost exclusively on the Si-rich side of the interface.

The structure of the interface in the 150–106-µm drop-tube sample is less easy to categorise as it does not easily fit into the standard descriptions of being coherent, semi-coherent or incoherent. What we appear to have is a change in growth direction from < 220 > in the Si-rich material to < 111 > in the Ge-rich material, with the angle between the (111) and (220) planes being very similar to that expected in the case of there being a common underlying crystallography. As such, we would most acurately describe the interface between the Ge-deficient and Ge-rich material in this sample as representing a change in growth direction. However, as with the other samples, the interface is diffuse, with the < 111 > growth direction of the Ge-rich material extending 5–7 nm into the Ge-deficient material before a switch to < 220 > growth is apparent along the full field of view in the micrograph. Unlike the two more slowly cooled samples, in which the EDX and GPA strain maps revealed a coincident, sharp linear interface between the two phases, in the case of the most rapidly solidified material the interface revealed by the GPA strain mapping is more diffuse than that in the EDX maps, which like the other samples is near atomically sharp. Moreover, in this rapidly cooled sample, there are virtually no dislocations visible on either side of the interface.

The lattice mismatch across the interfaces, as evaluated using Eq. (5) which is based upon the lattice parameter a, so as to factor out any change in growth diretion, is 7.9%, −4.2% and 2.1% for the crucible residue, > 850 µm and 150–106 µm samples respectively, compared with predictions based on Vegard's law with the compositions observed at these step-mediated boundaries of 0.78%, 1.8% and 2.3%. These values have a relatively high uncertainty in the case of the crucible residue and > 850-µm drop-tube sample, due to the high density of dislocations giving a high degree of variability in the measured lattice spacing for these two samples. This is particularly the case for the > 850-µm sample where the lattice strain is measured as negative due to an anomalously high lattice parameter on the Si-rich side of the step-mediated concentration interface. Nonetheless, the evidence, particularly the drop in strain between the near equilibrium crucible residue sample and the rapidly solidified 150–106-µm drop-tube sample is suggestive that the change in growth direction may be acting so as to minimise lattice mismatch across the interface. However, this does seemingly conflict with the GPA analysis which indicates a larger strain jump in the case of the 150–106-µm sample, relative to either of the slower cooled samples, this being from an average for the "speckle" pattern of around + 0.02 on the Si-rich side of the interface in all three cases to −0.1 on the Ge-rich side of the 150–106-µm sample compared to values close to zero in the two slower cooled samples.

Returning to the distribution of dislocations, we may postulate two alternative mechanisms which gives rise to these being located predominantly on the Si-rich side of the step-mediated interfaces in the crucible residue and > 850-µm drop-tube samples. The first of these relates to the elastic properties of the materials on either side of the interface, wherein we may postulate that the elastic properties are such as to naturally favour dislocations being located in the Ge-deficient material as a means of minimising the free energy of the system. Alternatively, we may appeal to a temporal mechanism, based upon the known solidification path. We know that during solidification, Ge will be rejected from the growing solid throughout solidification. Consequently, irrespective of the solid fraction, the material on the Ge-rich side of an interface is solidifying later than the Ge-deficient material on the other side of that interface. Moreover, the liquid will be becoming progessively more Ge-rich, even if the solid as it forms does so at the same composition as the previous solid. Therein, we may postulate that just prior to a step-mediated change in the concentration of the solid, a high density of dislocations are being incorporated into that solid. At some point that density of dislocations becomes such, that a step change in concentration becomes favoured for the newly growing solid, with a reduction in strain such that this new, more Ge-rich, solid can form with a much lower dislocation density.

These two alternatives are testable as, in the case of the distribution of dislocations being determined soely by the elastic properties of the material on either side of the interface, this difference in dislocation density can be estimated based upon the energy, E, required to form the dislocation. This in turn can be expressed in terms of the elastic constants for the material, namely C_{11}, C_{12} and C_{44}. As far as we are aware, these have not been determined for Si-Ge alloys, but are well documented for the pure elements. In this work we have assumed that the elastic properties of the Si-Ge alloys can be approximated by a compositionally weighted average of the value for the pure elements, with these being given in Table 2. E is then given by:

$$E = \frac{Gb^2}{2(1-\upsilon)} \tag{7}$$

where G is the shear modulus, b is the Burgers vector and υ is Poisson's ratio. For the diamond cubic crystal system these may be approximated as $G = C_{44}$, $\upsilon = C_{12}/(C_{11} - C_{12})$ and $b = \sqrt{3}a/2$, with a being the lattice parameter. From this, the density of dislocations, ρ_{dis}, follows as:

$$\rho_{\text{dis}} = \frac{1}{b^2}\exp\left\{-\frac{2\alpha - 4\pi(1-\upsilon)}{(1-0.5\upsilon)}\right\} \tag{8}$$

where α is a parameter in the range 0.5–1.5 [54,55] although it is usually considered constant regardless of the degree of deformation of the material.

From Eqs. (7–8), and using the values given in Table 2, we estimate that for the crucible residue, in which the Ge-concentration jumps from 6 to 24 at% Ge, the dislocation energy is 18.99 eV on the Si-rich side and 19.04 eV on the Ge-rich side, with corresponding dislocation densities of 3.88×10^{11} m^{-2} and 3.31×10^{11} m^{-2} respectively. In the > 850-µm drop-tube sample, in which the concentration jump is from 25 to 67 at% Ge, the dislocation energies are 25.15 eV and 20.25 eV while the corresponding dislocation densities are 2.94×10^{11} m^{-2} and 3.20×10^{11} m^{-2} on the Si-rich and Ge-rich sides of the interface respectively. In both samples, we therefore predicted that, based on the elastic properties of the material, there should be no more than a 15% difference in the density of dislocations on either side of the interface. We do not believe that this is consistent with the observed, almost exclusive presence of dislocations on the Si-rich side of the interface in the crucible residue and > 850-µm sample and conclude that it is more likely the temporal order that the material is formed in, rather than the elastic properties of the material *per se*, that are determining the observed distribution of dislocations. As such, the increased density of dislocations would be a precursor to a step-mediated change in concentration, indicative of a high level of accumualted strain within lattice.

Rapid solidification, which in most materials would result in greater chemical homogeneity, was conversely in this work found to produce multiple discrete SiGe compositions. Such grain boundaries, phase interfaces, and compositional fluctuations can act as scattering centers for phonons, thereby reducing lattice thermal conductivity [56,57]. While this reduction can benefit thermoelectric efficiency, literature also shows that excessive grain boundary scattering can significantly impede charge-carrier mobility and lower electrical conductivity, thereby degrading the overall thermoelectric power factor [58–60]. In polycrystalline thermoelectrics, grain boundaries may introduce potential barriers and trap sites, causing carrier mobility losses that outweigh gains from reduced thermal conductivity [58–60]. Previous studies indicate that optimal performance requires controlling the density, distribution, and nature of scattering sites to balance phonon and electron scattering [56–60].

Although, due to the large grain size of the Si-rich grains, the volume fraction of Si-rich/Ge-rich interfaces in the present samples is relatively small compared to nanostructured thermoelectrics, their influence on

Table 2
Elastic constants of pure Si and pure Ge [52,53].

Material	C_{11} (GPa)	C_{12} (GPa)	C_{44} (GPa)
Si	165.7	63.9	79.6
Ge	128.9	48.3	67.1

physical properties is likely to be non-negligible. In particular, interfaces displaying a significant step-change in composition, as found in this study, are likely to have a larger effect on both photon and phonon scattering than if a similar composition change occurred continuously, as predicted by the phase diagram. For instance, in thin films Kadri, et al. [61] have shown that a step-change in composition of 15 at%-Ge can result in a refractive index at the interface of 0.8. Moreover, the large difference in lattice parameter (~4.2%) and mass density between Si-rich and Ge-rich regions can produce substantial phonon scattering, especially for long-wavelength phonons whose mean free paths are on the order of the observed interface spacing. The present microstructural insights into rapid solidification may therefore provide a basis for guiding future work aimed at correlating specific microstructural scattering sources with thermoelectric performance.

4. Conclusions

Step-mediated partitioning is demonstrated in a Si-30wt%Ge thermoelectric alloy solidified from its parent melt, with a range of discrete compositions being observed in the Ge-rich grain boundary regions. Moreover, in drop-tube processed samples, the heterogeneity in the material increases as the cooling rate increases, with smaller but more Ge-rich grain boundary regions and larger concentration steps. Such step-mediated concentration gradients are well documented in Si-Ge thin films [19,20], where the phenomenon is explained as a mechanism to relieve the lattice strain arising from the large difference in atomic radius between Si and Ge. In thin films it is postulated that chemical ordering on at least one side of the interface is a necessary condition for step-mediated solute segregation [19] and this is also observed in our bulk samples. Moreover, the discrete compositions we observe seem to be multiples of 5 at%, a phenomenon that would most naturally be explained by supercell ordering of the Si-Ge diamond cubic cells.

HRTEM imaging of three step-mediated interfaces reveal that at low to intermediate cooling rates there is a high density of dislocations on the Si-rich side of the interface while in the most rapidly cooled sample there appears to be a change in growth direction at the interface, which we suggest is a means of minimising the strain at the interface. Strain determination at all three interfaces, using both manual lattice strain determination and GPA, is consistent with this interpretation, with strain increasing with cooling rate whilst the same growth orientation is maintained at the interface, but with a lower strain observed once a change in growth orientation occurs. Taken together, the results have significant implications for the fabrication of Si–Ge thermoelectric devices, where a high degree of chemical homogeneity is essential for optimum performance. Although heterogeneity increases with rapid solidification, step-mediated concentration gradients are also observed close to equilibrium, signifying a fundamental limitation in producing homogeneous Si–Ge from the melt.

CRediT authorship contribution statement

Osama Al-Jenabi: Writing – original draft, Validation, Resources, Methodology, Investigation, Data curation, Conceptualization. **Ahmed Nassar:** Methodology. **Robert F. Cochrane:** Resources, Methodology, Conceptualization. **Andrew M. Mullis:** Writing – review & editing, Resources, Methodology, Data curation, Conceptualization.

Declaration of Competing Interest

The authors declare that they have no known competing financial interests or personal relationships that could have appeared to influence the work reported in this paper.

Acknowledgements

Al-Jenabi would like to thank the Republic of Iraq, the Ministry of Higher Education and Scientific Research, University of Anbar for their financial support (Grant Number: F.A.\5940:30/11/2020). The authors gratefully acknowledge LEMAS for their support & assistance in this work.

Appendix A. Supporting information

Supplementary data associated with this article can be found in the online version at doi:10.1016/j.jallcom.2026.187626.

References

[1] R. Ahuja, C. Persson, A. Ferreira da Silva, J. Souza de Almeida, C. Moyses Araujo, B. Johansson, Optical properties of SiGe alloys, J. Appl. Phys. 93 (2003) 3832–3836, https://doi.org/10.1063/1.1555702.

[2] K. Ismail, S. Nelson, J. Chu, B. Meyerson, Electron transport properties of Si/SiGe heterostructures: measurements and device implications, Appl. Phys. Lett. 63 (1993) 660–662, https://doi.org/10.1063/1.109949.

[3] B. Cai, H. Hu, H.-L. Zhuang, J.-F. Li, Promising materials for thermoelectric applications, J. Alloy. Compd. 806 (2019) 471–486, https://doi.org/10.1016/j.jallcom.2019.07.147.

[4] N. Hussain, A.M. Mullis, N. Haque, Effect of cooling rate on the microstructure of rapidly solidified SiGe, Mater. Charact. 154 (2019) 377–385, https://doi.org/10.1016/j.matchar.2019.06.014.

[5] J. Li, C. Zhao, Y. Xing, S. Su, B. Cheng, Full-field strain mapping at a Ge/Si heterostructure interface, Materials 6 (2013) 2130–2142, https://doi.org/10.3390/ma6062130.

[6] L. Li, Z. Chen, M. Zhou, R. Huang, Developments in semiconductor thermoelectric materials, Front. Energy 5 (2011) 125–136, https://doi.org/10.1007/s11708-011-0150-1.

[7] O. Al-Jenabi, Z. Aslam, R.F. Cochrane, A.M. Mullis, Microstructural characterisation and compound formation in rapidly solidified SiGe alloy, J. Alloy. Compd. 992 (2024) 174560, https://doi.org/10.1016/j.jallcom.2024.174560.

[8] N. Hussain, A. Mullis, Microstructure characterisation of drop tube processed SiGe semiconductor alloy, in: Proceedings of the 7th International Conference on Solidification & Gravity 2018, Leeds, 2018, pp. 291–296. ⟨https://eprints.whiterose.ac.uk/id/eprint/135637/⟩.

[9] P. Zhang, Z. Wang, H. Chen, H. Yu, L. Zhu, X. Jian, Effect of cooling rate on microstructural homogeneity and grain size of n-Type Si-Ge thermoelectric alloy by melt spinning, J. Electron. Mater. 39 (2010) 2251–2254, https://doi.org/10.1007/s11664-010-1314-1.

[10] A. Gumennik, E.C. Levy, B. Grena, C. Hou, M. Rein, A.F. Abouraddy, J. D. Joannopoulos, Y. Fink, Confined in-fiber solidification and structural control of silicon and silicon− germanium microparticles, Proc. Natl. Acad. Sci. U. S. A. 114 (2017) 7240–7245, https://doi.org/10.1073/pnas.1707778114.

[11] L. Goldman, M. Aziz, Aperiodic stepwise growth model for the velocity and orientation dependence of solute trapping, J. Mater. Res. 2 (1987) 524–527, https://doi.org/10.1557/jmr.1987.0524.

[12] P. Evans, G. Devaud, T. Kelly, Y.-W. Kim, Solidification of highly undercooled Si and Ge droplets, Acta Metall. Mater. 38 (1990) 719–726, https://doi.org/10.1016/0956-7151(90)90023-a.

[13] R. Welch, B. Şişik, S. LeBlanc, Micro-and nano-structures formed in silicon germanium undergoing laser melting for additive manufacturing, JOM 77 (2025) 793–808, https://doi.org/10.1007/s11837-024-06941-4.

[14] A. Ghosh, W. Wu, T. Ma, A.J. Shahani, J. Wang, A. Misra, Systematic discovery of new nano-scale metastable intermetallic eutectic phases in laser rapid solidified Aluminum-Germanium alloy, J. Alloy. Compd. 1011 (2025) 178413, https://doi.org/10.1016/j.jallcom.2024.178413.

[15] A. Ghosh, W. Wu, J. Wang, A. Misra, High strength ultrafine eutectic composites with metastable intermetallic phases, J. Mater. Sci. Technol. 235 (2025) 174–188, https://doi.org/10.1016/j.jmst.2025.03.019.

[16] P. Tomasini, A simplified model for the vapor–solid distribution of silicon germanium chemical vapor deposition, Mater. Sci. Semicond. Process 125 (2021) 105649, https://doi.org/10.1016/j.mssp.2020.105649.

[17] C. Lang, The interdependency of morphology, strain and composition in buried GeSi/Si (001) quantum dots, Philos. Mag. 90 (2010) 4703–4709, https://doi.org/10.1080/14786435.2010.489888.

[18] X. Li, Y. Ouyang, R. Zhang, X. Tao, Y. Geng, S. Li, Y. Zhang, H. Gao, Mapping of strain in multilayer GaAs/AlAs superlattices from HRTEM micrographs, Mater. Lett. 284 (2021) 129020, https://doi.org/10.1016/j.matlet.2020.129020.

[19] T. Araki, N. Fujimura, T. Ito, Mechanism for ordering in SiGe films with reconstructed surface, Appl. Phys. Lett. 71 (1997) 1174–1176, https://doi.org/10.1063/1.119617.

[20] E. Müllers, H.-U. Nissen, K. Mäder, M. Ospelt, H. Von Känel, Occurrence of two ordered structures in Si–Ge systems, Philos. Mag. Lett. 64 (1991) 183–189, https://doi.org/10.1080/09500839108214541.

[21] E. Guerrero, P. Galindo, A. Yáñez, T. Ben, S.I. Molina, Error quantification in strain mapping methods, Microsc. Micro 13 (2007) 320–328, https://doi.org/10.1017/s1431927607070407.

[22] O. Oloyede, T.D. Bigg, R.F. Cochrane, A.M. Mullis, Microstructure evolution and mechanical properties of drop-tube processed, rapidly solidified grey cast iron, Mater. Sci. Eng. A 654 (2016) 143–150, https://doi.org/10.1016/j.msea.2015.12.020.

[23] O.I.A. Al-Jenabi, Rapid Solidification via Drop-Tube Processing of Si-Ge Thermoelectric Alloy, Ph.D. thesis, University of Leeds, 2025. ⟨https://etheses.whiterose.ac.uk/id/eprint/37054/⟩.

[24] M. Hÿtch, E. Snoeck, R. Kilaas, Quantitative measurement of displacement and strain fields from HREM micrographs, Ultramicroscopy 74 (1998) 131–146, https://doi.org/10.1016/s0304-3991(98)00035-7.

[25] E. Kasper, A. Schuh, G. Bauer, B. Holländer, H. Kibbel, Test of Vegard's law in thin epitaxial SiGe layers, J. Cryst. Growth 157 (1995) 68–72, https://doi.org/10.1016/0022-0248(95)00373-8.

[26] T. Taniguchi, T. Ishibe, N. Naruse, Y. Mera, M.M. Alam, K. Sawano, Y. Nakamura, High thermoelectric power factor realization in Si-rich SiGe/Si superlattices by super-controlled interfaces, ACS Appl. Mater. Interfaces 12 (2020) 25428–25434, https://doi.org/10.1021/acsami.0c04982.

[27] P. Algoso, W. Hofmeister, R. Bayuzick, Solidification velocity of undercooled Ni–Cu alloys, Acta Mater. 51 (2003) 4307–4318, https://doi.org/10.1016/s1359-6454(03)00257-x.

[28] X.J. Han, C. Yang, B. Wei, M. Chen, Z.Y. Guo, Rapid solidification of highly undercooled Ni–Cu alloys, Mater. Sci. Eng. A 307 (2001) 35–41, https://doi.org/10.1016/s0921-5093(00)01969-9.

[29] H. Wang, Y. An, X. Xu, X. Guo, Y. Hu, Rapid solidification microstructure evolution and grain refinement of deeply undercooled nickel alloys, Mater. Charact. 170 (2020) 110703, https://doi.org/10.1016/j.matchar.2020.110703.

[30] L. Wang, X.-F. Bian, J.-X. Zhang, Rapid solidification and crystal growth of Au3Ag alloy by MD simulation, Mater. Sci. Eng. A 298 (2001) 262–267, https://doi.org/10.1016/s0921-5093(00)01224-7.

[31] A.Y. Volkov, P. Podgorbunskaya, O. Novikova, A. Valiullin, A. Glukhov, N. Kruglikov, Atomic ordering kinetics in a Cu–56 at% Au alloy at a temperature of 250° C, Inorg. Mater. 59 (2023) 563–569, https://doi.org/10.1134/s0020168523060171.

[32] F. Hüe, M. Hÿtch, H. Bender, F. Houdellier, A. Claverie, Direct mapping of strain in a strained silicon transistor by high-resolution electron microscopy, Phys. Rev. Lett. 100 (2008) 156602, https://doi.org/10.1103/physrevlett.100.156602.

[33] J. Madsen, P. Liu, J.B. Wagner, T.W. Hansen, J. Schiøtz, Accuracy of surface strain measurements from transmission electron microscopy images of nanoparticles, Adv. Struct. Chem. Imaging 3 (2017) 14, https://doi.org/10.1186/s40679-017-0047-0.

[34] L. Li, R. Bi, Z. Dong, C. Ye, J. Xie, C. Wang, X. Li, K.L. Pey, M. Li, X. Wu, Atomic-scale strain analysis for advanced Si/SiGe heterostructure by using transmission electron microscopy, Electron 2 (2024) e32, https://doi.org/10.1186/s40679-017-0047-0.

[35] M.A. Hopcroft, W.D. Nix, T.W. Kenny, What is the Young's Modulus of Silicon? J. Micro Syst. 19 (2010) 229–238, https://doi.org/10.1109/jmems.2009.2039697.

[36] F.W. DelRio, R.F. Cook, B.L. Boyce, Fracture strength of micro-and nano-scale silicon components, Appl. Phys. Rev. 2 (2015) 021303, https://doi.org/10.1063/1.4919540.

[37] R. Cook, Strength and sharp contact fracture of silicon, J. Mater. Sci. 41 (2006) 841–872, https://doi.org/10.1007/s10853-006-6567-y.

[38] G. Stan, S. Krylyuk, A. Davydov, I. Levin, R.F. Cook, Ultimate bending strength of Si nanowires, Nano Lett. 12 (2012) 2599–2604, https://doi.org/10.1021/nl300957a.

[39] H. Zhang, J. Tersoff, S. Xu, H. Chen, Q. Zhang, K. Zhang, Y. Yang, C.-S. Lee, K.-N. Tu, J. Li, Approaching the ideal elastic strain limit in silicon nanowires, Sci. Adv. 2 (2016) e1501382, https://doi.org/10.1126/sciadv.1501382.

[40] S.-M. Dubois, G.-M. Rignanese, T. Pardoen, J.-C. Charlier, Ideal strength of silicon: an ab initio study, Phys. Rev. B 74 (2006) 235203, https://doi.org/10.1103/physrevb.74.235203.

[41] P. Németh, K. McColl, L.A. Garvie, C.G. Salzmann, M. Murri, P.F. McMillan, Complex nanostructures in diamond, Nat. Mater. 19 (2020) 1126–1131, https://doi.org/10.1038/s41563-020-0759-8.

[42] M.J. Aziz, Non-equilibrium interface kinetics during rapid solidification, Mater. Sci. Eng. A 178 (1994) 167–170, https://doi.org/10.1016/0921-5093(94)90537-1.

[43] S. Sobolev, Local-nonequilibrium model for rapid solidification of undercooled melts, Phys. Lett. A 199 (1995) 383–386, https://doi.org/10.1016/0375-9601(95)00084-g.

[44] P. Galenko, Solute trapping and diffusionless solidification in a binary system, Phys. Rev. E 76 (2007) 031606, https://doi.org/10.1103/physreve.76.031606.

[45] A.M. Mullis, O.E. Jegede, T.D. Bigg, R.F. Cochrane, Dynamics of core–shell particle formation in drop-tube processed metastable monotectic alloys, Acta Mater. 188 (2020) 591–598, https://doi.org/10.1016/j.actamat.2020.02.017.

[46] W. Nan, W. Bing-Bo, Droplet undercooling during containerless processing in a DropTube, Chin. Phys. Lett. 21 (2004) 1120, https://doi.org/10.1088/0256-307x/21/6/040.

[47] C. Panofen, D. Herlach, Solidification of highly undercooled Si and Si–Ge melts, Mater. Sci. Eng. A 449 (2007) 699–703, https://doi.org/10.1016/j.msea.2006.02.443.

[48] D. Brunco, M.O. Thompson, D. Hoglund, M. Aziz, H.J. Gossmann, Germanium partitioning in silicon during rapid solidification, J. Appl. Phys. 78 (1995) 1575–1582, https://doi.org/10.1063/1.360251.

[49] W. Boettinger, M. Aziz, Theory for the trapping of disorder and solute in intermetallic phases by rapid solidification, Acta Met. 37 (1989) 3379–3391, https://doi.org/10.1016/0001-6160(89)90210-1.

[50] N. Haque, R.F. Cochrane, A.M. Mullis, Rapid solidification morphologies in Ni3Ge: spherulites, dendrites and dense-branched fractal structures, Intermetallics 76 (2016) 70–77, https://doi.org/10.1016/j.intermet.2016.06.012.

[51] A.M. Mullis, N. Haque, Evidence for dendritic fragmentation in as-solidified samples of deeply undercooled melts, J. Cryst. Growth 529 (2020) 125276, https://doi.org/10.1016/j.jcrysgro.2019.125276.

[52] A. George, Elastic constants and moduli of diamond cubic Si, in: R. Hull (Ed.), Properties of Crystalline Silicon, INSPEC, IEE, London, 1999, pp. 144–148.

[53] S. Muramatsu, M. Kitamura, Simple expressions for elastic constants c11, c12, and c44 and internal displacements of semiconductors, J. Appl. Phys. 73 (1993) 4270–4272, https://doi.org/10.1063/1.352807.

[54] J. Humphreys, G.S. Rohrer, A. Rollett, Recrystallization textures, in: Recrystallization and Related Annealing Phenomena, 3rd ed., Elsevier, Oxford, 2017, pp. 431–468, https://doi.org/10.1016/b978-0-08-098235-9.00012-4.

[55] J.J. Sidor, P. Chakravarty, J.G. Bátorfi, P. Nagy, Q. Xie, J. Gubicza, Assessment of dislocation density by various techniques in cold rolled 1050 aluminum alloy, Metals 11 (2021) 1571, https://doi.org/10.3390/met11101571.

[56] K. Biswas, J. He, Q. Zhang, G. Wang, C. Uher, V.P. Dravid, M.G. Kanatzidis, Strained endotaxial nanostructures with high thermoelectric figure of merit, Nat. Chem. 3 (2011) 160–166, https://doi.org/10.1038/nchem.955.

[57] C.J. Vineis, A. Shakouri, A. Majumdar, M.G. Kanatzidis, Nanostructured thermoelectrics: big efficiency gains from small features, Adv. Mater. 22 (2010) 3970–3980, https://doi.org/10.1002/adma.201000839.

[58] C. Hu, K. Xia, C. Fu, X. Zhao, T. Zhu, Carrier grain boundary scattering in thermoelectric materials, Energy Environ. Sci. 15 (2022) 1406–1422, https://doi.org/10.1039/d1ee03802h.

[59] Y. Li, T. Hong, X. Li, H. An, Z. Yin, M. Wu, H. Liang, X. Wang, L. Su, X. Qian, C. Zhou, Mass transport and grain growth enable high thermoelectric performance in polycrystalline SnS, J. Mater. Chem. A 13 (2025) 2904–2914, https://doi.org/10.1039/d5ta05300e.

[60] M. Markwitz, P.P. Murmu, S.Y. Back, T. Mori, B.J. Ruck, J. Kennedy, Effect of grain boundary scattering on carrier mobility and thermoelectric properties of tellurium incorporated copper iodide thin films, Surf. Interfaces 41 (2023) 103190, https://doi.org/10.1016/j.surfin.2023.103190.

[61] E. Kadri, M. Krichen, S. Elleuch, A.B. Arab, Optical properties of Si1− xGex/Si thin films, Opt. Quantum Electron 48 (2016) 352, https://doi.org/10.1007/s11082-016-0630-y.